Supplementary Notes for the article "Micro-scale dissolution seams mobilise carbon in deep-sea limestones"

Christoph E. Schrank[1*], Michael M. W. Jones[2*], Cameron M. Kewish[3], Grant A. van Riessen[4], Kathryn E. Elphick[1], Craig R. Sloss[1], Luke D. Nothdurft[1], Gregory E. Webb[5], David J. Paterson[3], and Klaus Regenauer-Lieb[6]

[1]Queensland University of Technology, School of Earth and Atmospheric Sciences, 2 George St, Brisbane, 4000, QLD, Australia
[*]Corresponding author: christoph.schrank@qut.edu.au
[2]Queensland University of Technology, Central Analytical Research Facility, 2 George St, Brisbane, 4000, QLD, Australia
[*]Corresponding author: mw.jones@qut.edu.au
[3]Australian Synchrotron, 800 Blackburn Rd, Clayton, 3168, VIC, Australia
[4]La Trobe University, Chemistry and Physics, La Trobe Institute for Molecular Science, Melbourne, 3086, VIC, Australia
[5]University of Queensland, School of Earth and Environmental Sciences, St. Lucia, 4067, QLD, Australia
[6]The University of New South Wales, School of Minerals and Energy Resources Engineering, Anzac Parade, Kensington, 2033, NSW, Australia

Supplementary Note 1: Geological background

Geological Setting

The studied Paleocene[1] limestone package is part of the Kaiwhata Formation[2] and crops out in coastal exposures near the Pahaoa river mouth in the Wairarapa region of the North Island of New Zealand (Supplementary Figure 1). The Kaiwhata limestones have a total thickness of ca. 34 m in the research area and consist of decimetric layers of calci-mudstones and wackestones *sensu* Wright[3] with intercalated centi- to decimetric sand- and siltstones (Fig. 1a). They are conformably underlain by shales and sandstones of Late-Cretaceous age and overlain by a ca. 31-m-thick unit of Eocene mudstone[1]. These three rock packages are interpreted as a deep-marine passive-margin sequence, which is conformably capped by an early-Miocene olistostrome deposit heralding the onset of the Hikurangi subduction[1]. The subduction process entrained the Pahaoa limestones into the accretionary wedge of the Hikurangi margin. They currently constitute a part of the exhumed inner wedge[4]. During their ca. 25 Myr long journey from the seafloor through the wedge back to the surface, the Kaiwhata limestones experienced three deformation events[4]. The first deformation event (D1) began with the onset of subduction and involves a ca. 5 Myr long period of trench-perpendicular horizontal contraction, accommodated by the emplacement of sub-horizontal thrust sheets, reverse faulting, and folding[5,6]. Synsedimentary plastic deformation structures of Kaiwhata-limestone clasts within the overlying olistostrome indicate that the limestones were not yet completely lithified at that time[1]. From the middle to late Miocene, between ca. 15 and 5 Myr ago, the wedge experienced wide-spread horizontal extension indicated by trench-parallel and -perpendicular normal faulting, possibly due to tectonic erosion[4,6]. This second deformation event (D2) imprinted brittle normal faults with a dominantly north-westerly strike into the Kaiwhata limestones (Supplementary Figure 1). The final event (D3) is ongoing and characterised by trench-perpendicular horizontal contraction of the wedge, which resulted in kilometre-scale trenchward verging north-east striking folds and thrusts in the research area (Supplementary Figure 1)[1,4]. Regional burial estimates from the Wairarapa region[7] and petrophysical properties of the conformably overlying Miocene Whakataki Formation indicate that maximum burial depth of the Pahaoa limestones did not exceed 3000 m. The associated maximum burial temperature is likely $\leq 115°C$[8]. These depth and temperature estimates are consistent[9] with the high smectite content[1] of the Eocene mudstones capping the limestone sequence.

Supplementary Note 2: Escape Depth of Fluorescent X-rays

The depth at which elements can be imaged in a specimen depends on the incident X-ray energy and the excited fluorescent X-ray energy. The incident energy must be high enough to penetrate the specimen to excite fluorescent photons. However, the depth at which the excited fluorescent photons can escape the specimen in order to be detected is strongly controlled by the element of interest. As excited fluorescent photons always have an energy less than the incident photon energy, the depth at which an excited fluorescent photon can escape to the detector is the limiting factor. We refer to the maximum depth, from which a fluorescent photon can escape, as the "accessible depth". Supplementary Table 1 provides an

estimation of the accessible depth for the most important elements considered in this study, using $CaCO_3$ with a density of 2.71 gcm^{-3} as matrix. Supplementary Figure 7 shows the corresponding accessible depth for $CaCO_3$ across the photon energy range up to the incident energy of 10keV[10].

Supplementary Table 1: Accessible depth for key elements of interest

Element	Accessible depth (μm)
Si	3.65
Ca	29.9
Ti	10.3
Fe	26.3

Supplementary Figures:

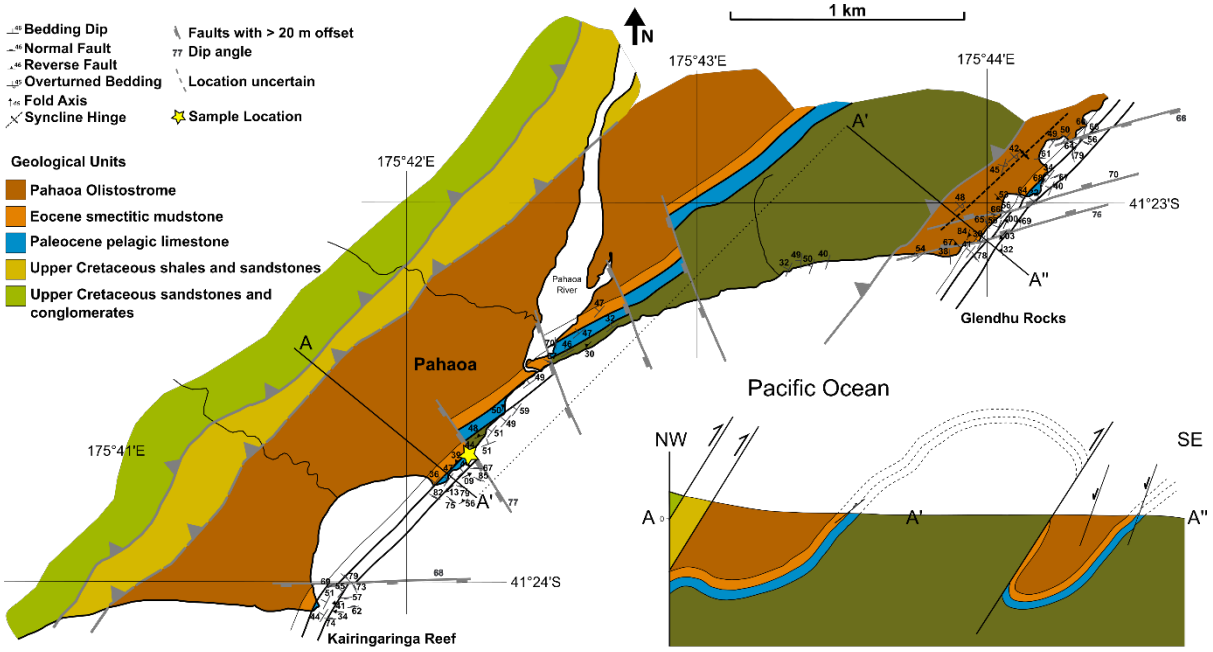

Supplementary Figure 1: Simplified interpreted geological map of the research area with composite cross-section, modified from Chanier and Ferrière[1] augmented by our own data. The samples come from the south-eastern limb of a D3 syncline. Sample-A coordinates: 41° 24" 20.28" S, 175° 42' 38.87" E (onshore exposure next two map label "Kairingaringa Reef"; map symbol not plotted to avoid obscuring of outcrop and orientation data). Sample-B coordinates (marked by yellow star): 41° 24' 0.26" S, 175° 43' 3.57" E.

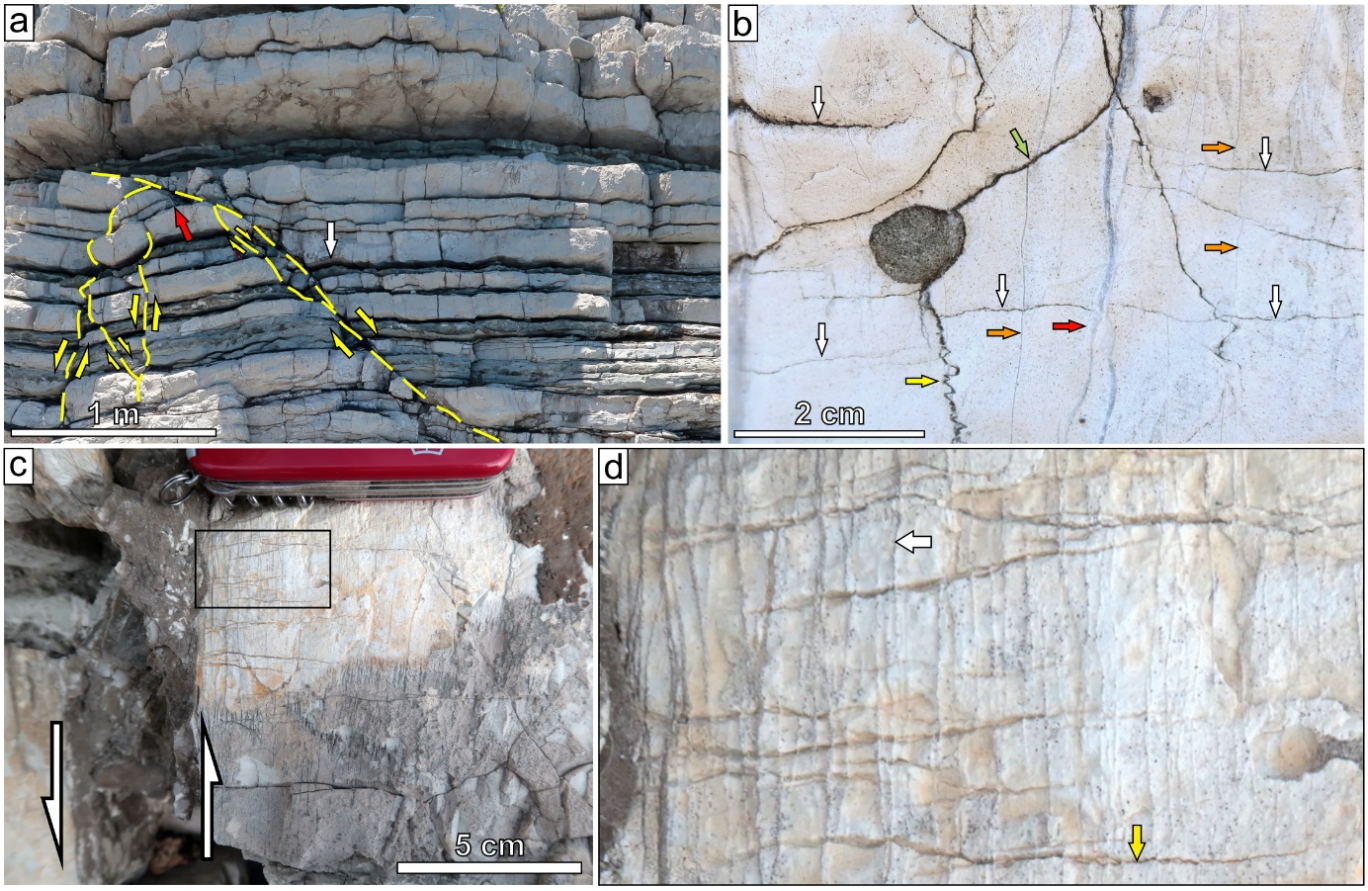

Supplementary Figure 2: Field examples demonstrating that diagenetic bedding-parallel stylolites are consistently cut by later deformation structures. Mutual overprint of bedding-parallel stylolites with bedding-perpendicular D2 veins would indicate syn-deformational D2 stylolite activity. However, this is not observed at the outcrop scale. Therefore, bedding-parallel stylolites, and in extension the micro-dissolution seams, must have formed during diagenesis. [a] Limestone outcrop with flat-lying beds displaying widespread diagenetic bedding-interface stylolites with sinusoidal geometry. A set of small D2 normal faults is traced with yellow dashed lines. These faults clearly truncate diagenetic stylolites (the white arrow highlights an example) and bend them in their associated drag folds (the red arrow marks an example). [b] Cross-sectional view of a horizontal wackestone bed. The white arrows mark bedding-parallel diagenetic stylolites with small roughness. They are cut consistently by bedding-perpendicular D2 calcite veins (a thick specimen is marked with the red arrow). The orange arrows mark D2 micro-veinlets, which all cut the horizontal diagenetic stylolites. Many of these micro-veinlets are much thinner than the diagenetic stylolites. Therefore, if the diagenetic stylolites would have accommodated any dissolution after emplacement of the veinlets, one would observe an offset of the veinlets. This is not the case. The yellow arrow marks a bedding-perpendicular, strongly serrated D1 stylolite. It clearly cuts and displaces the older generation of diagenetic horizontal stylolites but is cut by D2 veins, including D2 veinlets. The green arrow marks a D2 vein, which steps when cutting this stylolite (it could be mistaken for the opposite overprint). [c] Cross-sectional photograph of a wackestone bed cut by a small D2 normal fault decorated with secondary calcite (the fault boundaries are marked by the white shear-sense arrows). The D2 fault clearly cuts through bedding-parallel cm-scale diagenetic stylolites visible in the region underneath the pocketknife. The close-up shown in panel [d] is marked by the black rectangle. [d] D2 micro-veinlets parallel to the small fault in [c] (example marked with white arrow) consistently cut through the diagenetic stylolites (yellow arrow marks a specimen).

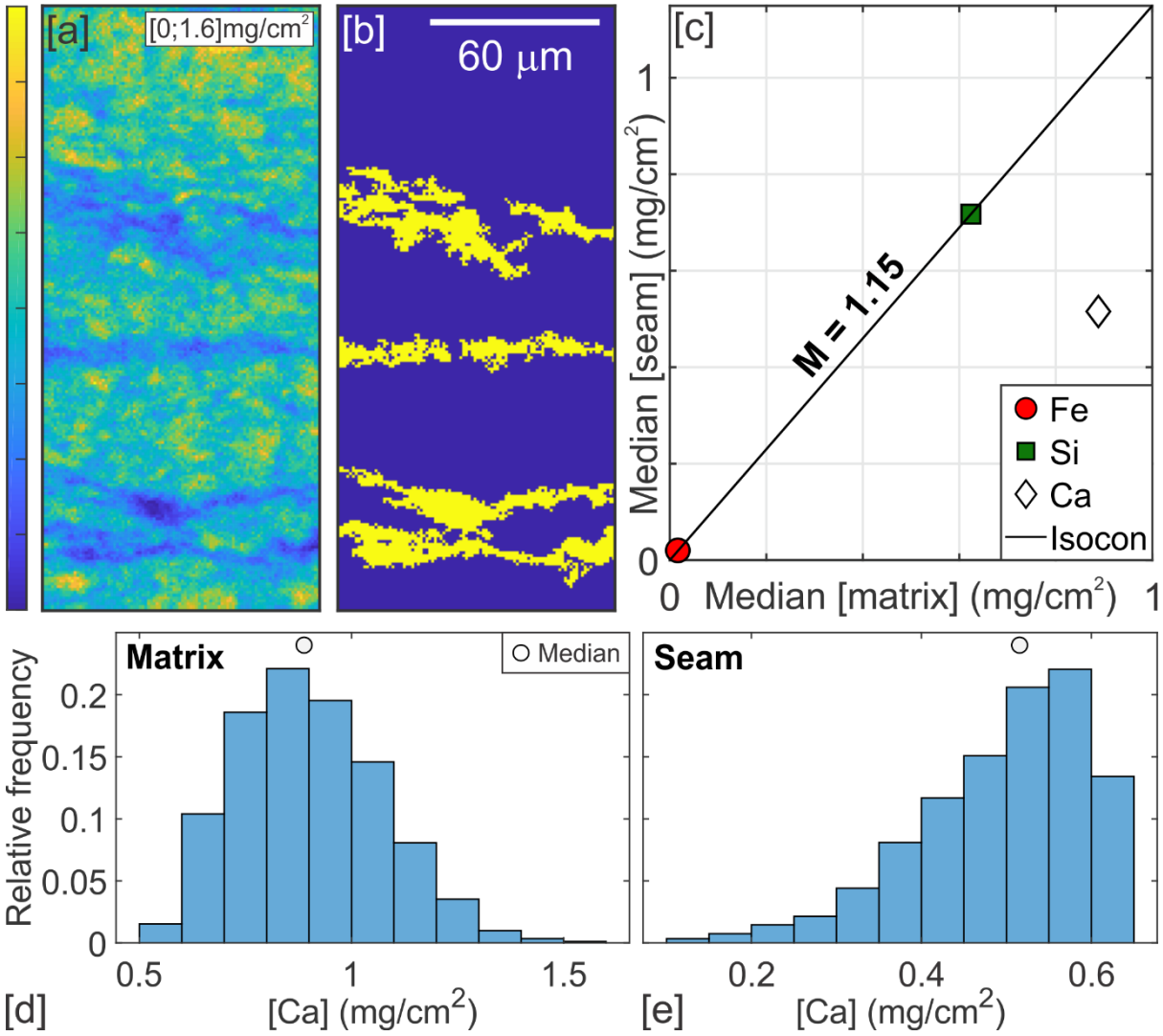

Supplementary Figure 3: Illustration of the Isocon method applied to a selected region of interest (ROI) in the XFM maps. [a] ROI of the Ca map. [b] Same map as in [a] after segmentation. Blue colour denotes unaltered matrix, yellow colour marks altered dissolution seams. [c] Isocon diagram for Ca, Fe, and Si with best-fit line to Eq. 2. The slope of this line gives M. [d] Relative frequency distribution of Ca concentration in the matrix. The circle marks the median used in the Isocon diagram shown in [c]. [e] Relative frequency distribution of Ca concentration in the micro-dissolution seams. The circle marks the median used in the Isocon diagram shown in [c].

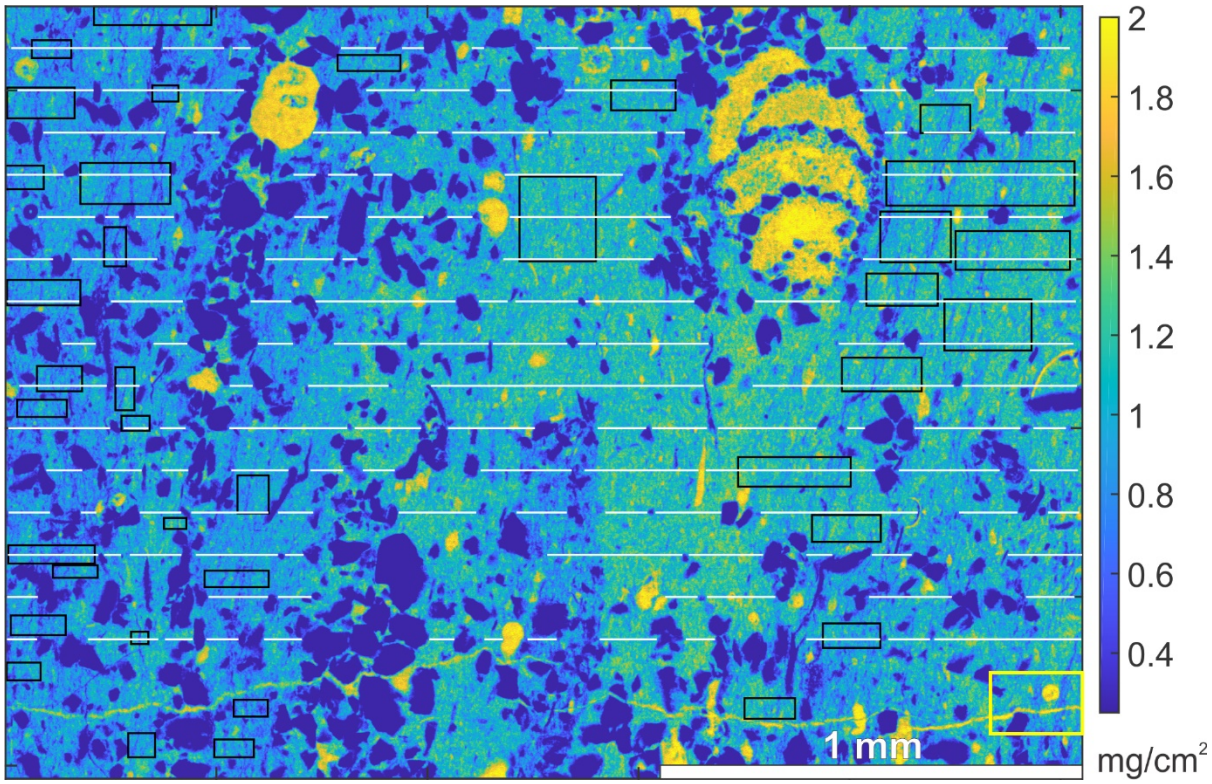

Supplementary Figure 4: Positions of ROIs (black rectangles) used in the Isocon analysis and scan-lines (white lines) examined for seam-width statistics and spatial frequencies plotted on the Ca map. Sedimentary bedding is vertical in this map. The thick yellow rectangle in the lower-right corner of the map marks an area where a D2 calcite vein (bright yellow) cuts through two micro-dissolution seams (dark blue).

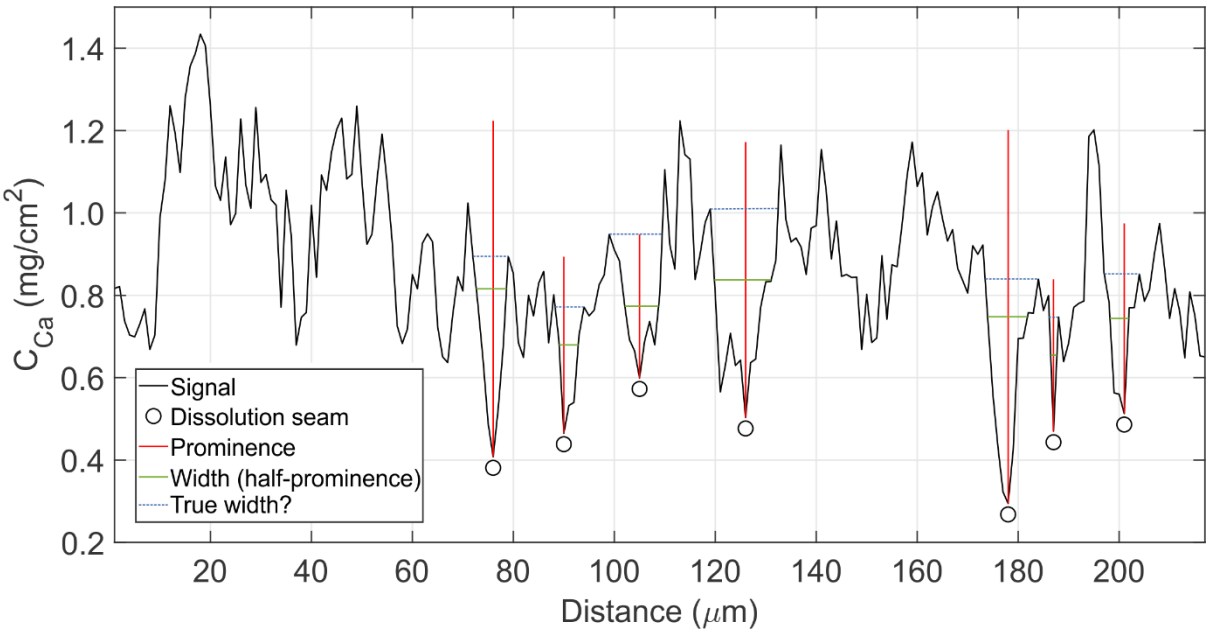

Supplementary Figure 5: Plot of the Ca profile along the second segment of the fourth scan-line (counted from map top) shown in Supplementary Figure 4. The white circles mark dissolution seams identified by the automated method described in the Methods section. Seam width at half-prominence (green lines) provides a conservative width estimate. Actual seam width may be larger. Horizontal blue dashed lines indicate width measured where the signal assumes its first maximum moving away from seam centre. With this criterion, seam width is generally larger than given by the half-prominence criterion.

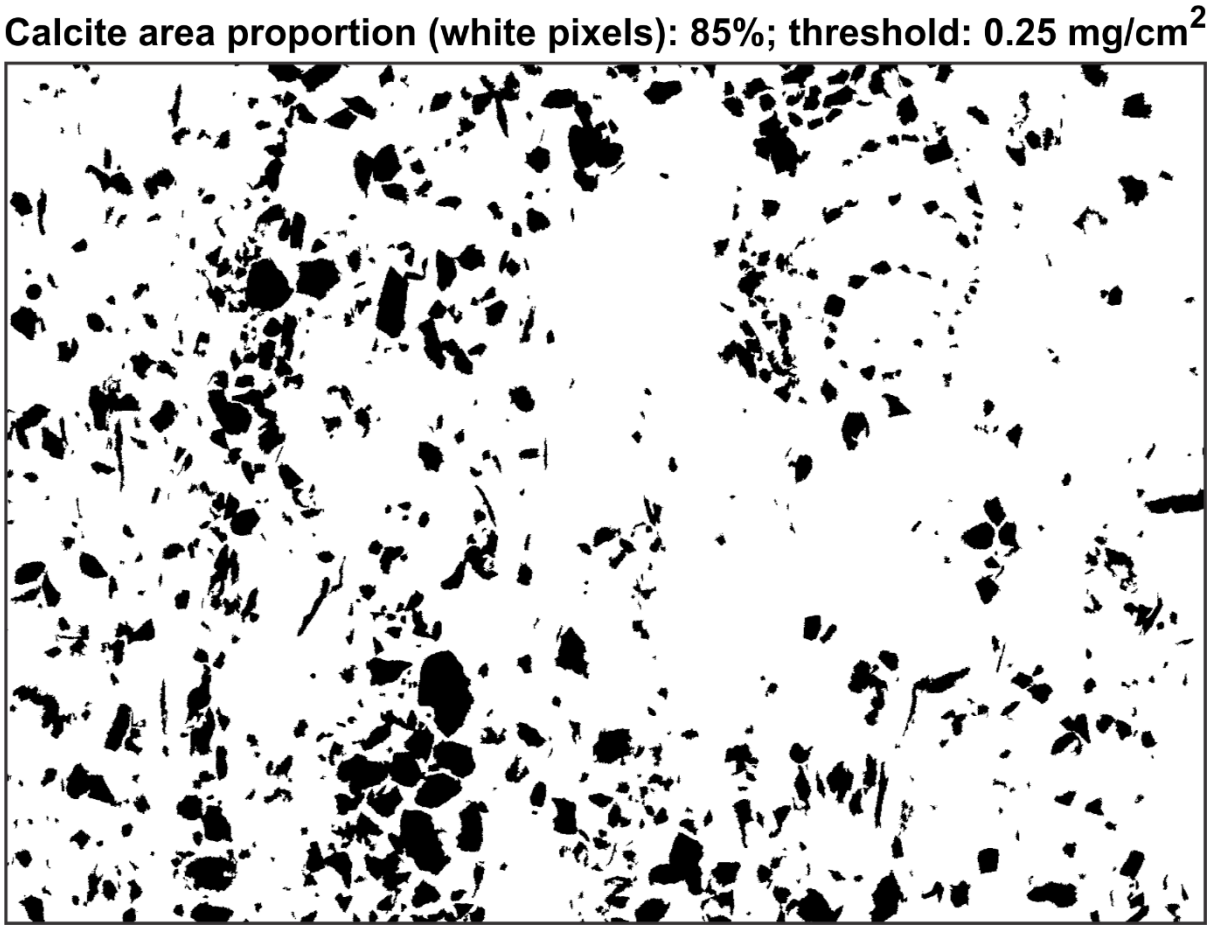

Supplementary Figure 6: Binary image derived from the XFM Ca map (Supplementary Figure 4), segmenting clastic detritus (black pixels) from Ca-rich, and thus calcitic, regions (white pixels). The sample contains ca. 15% detrital material by area.

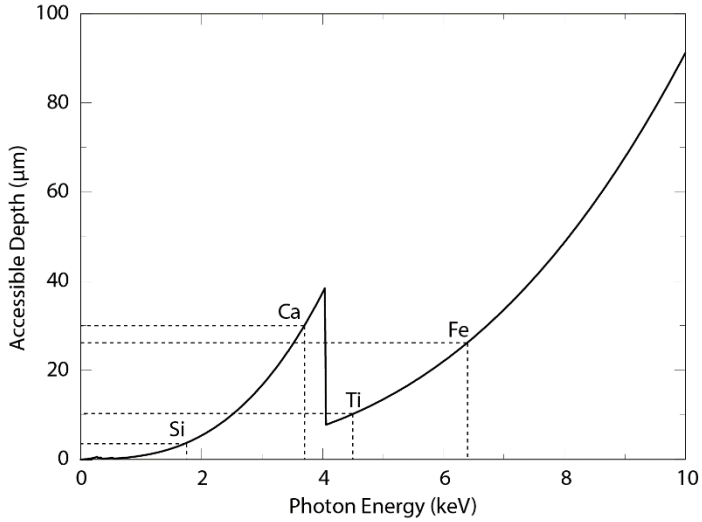

Supplementary Figure 7: Accessible depth for $CaCO_3$ (density 2.71gcm^{-3}) as function of the energy of the excited fluorescence photon. The large peak at ~4keV is the Ca absorption edge.

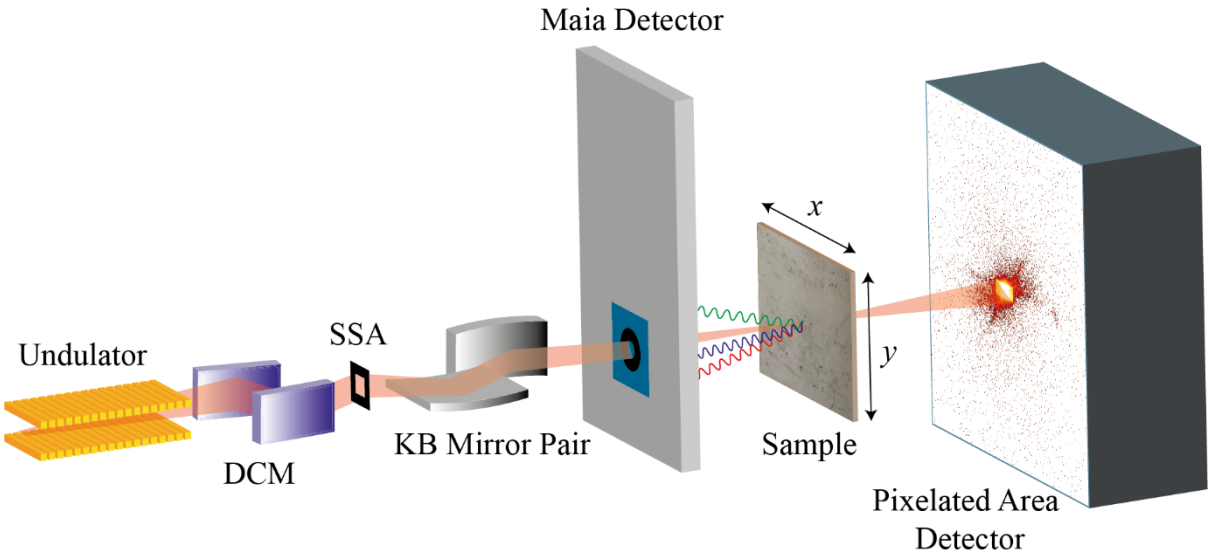

Supplementary Figure 8: The Experimental arrangement for simultaneous X-ray Fluorescence and X-ray ptychography data collection. An Undulator and Double Crystal Monochromator (DCM) produce monochromatic X-ray photons. A Secondary Source Aperture (SSA) defines the beam that is delivered to the Kirkpatrick-Baez (KB) Mirror Pair which produces a focus at the sample. The focused beam passes through a pinhole aperture and the Maia Detector before impinging on the sample. The sample is translated in the x- and y-directions while backscattered fluorescent X-ray photons are collected with the Maia Detector and the transmitted beam and diffracted photons are collected on a Pixelated Area Detector. Not to scale.

Supplementary References

1 Chanier, F. & Ferrière, J. From a passive to an active margin; tectonic and sedimentary processes linked to the birth of an accretionary prism (Hikurangi Margin, New Zealand). *Bulletin de la Societe Geologique de France* **162**, 649-660 (1991).

2 Van den Heuvel, H. B. The geology of the flat point area, eastern Wairarapa. *New Zealand Journal of Geology and Geophysics* **3**, 309-320, doi:10.1080/00288306.1960.10423603 (1960).

3 Wright, V. P. A revised classification of limestones. *Sedimentary Geology* **76**, 177-185, doi:https://doi.org/10.1016/0037-0738(92)90082-3 (1992).

4 Chanier, F. & Ferrière, J. Extensional deformation across an active margin, relations with subsidence, uplift, and rotations: The Hikurangi subduction, New Zealand. *Tectonics* **18**, 862-876 (1999).

5 Rait, G., Chanier, F. & Waters, D. Landward and seaward-directed thrusting accompanying the onset of subduction beneath New Zealand. *Geology* **19**, doi:10.1130/0091-7613(1991)019<0230:LASDTA>2.3.CO;2 (1991).

6 Bailleul, J. *et al.* Neogene evolution of lower trench-slope basins and wedge development in the central Hikurangi subduction margin, New Zealand. *Tectonophysics* **591**, 152-174, doi:http://dx.doi.org/10.1016/j.tecto.2013.01.003 (2013).

7 Wells, P. Burial history of Late Neogene sedimentary basins on part of the New Zealand convergent plate margin. *Basin Research* **2**, 145-160, doi:10.1111/j.1365-2117.1989.tb00032.x (1989).

8 Fukuchi, R., Yamaguchi, A., Yamamoto, Y. & Ashi, J. Paleothermal structure of the Nankai inner accretionary wedge estimated from vitrinite reflectance of cuttings. *Geochemistry, Geophysics, Geosystems* **18**, 3185-3196, doi:10.1002/2017GC006928 (2017).

9 Velde, B. & Vasseur, G. Estimation of the diagenetic smectite to illite transformation in time-temperature space. *American Mineralogist* **77**, 967-976 (1992).

10 Henke, B. L., Gullikson, E. M. & Davis, J. C. X-Ray Interactions: Photoabsorption, Scattering, Transmission, and Reflection at E = 50-30,000 eV, Z = 1-92. *Atomic Data and Nuclear Data Tables* **54**, 181-342, doi:https://doi.org/10.1006/adnd.1993.1013 (1993).